

REF: E3UB ISSUE: 1 Revision: 0 DATE: 27/3/2023

PAGE: 1









ESA Cloud_cci

End to End ECV Uncertainty Budget (E3UB)



Issue 1 Revision 0

27/3/2023

Deliverable No.: D2.2

ESRIN/Contract No.: 4000128637/20/I-NB Project Coordinator: Dr. Martin Stengel

Deutscher Wetterdienst martin.stengel@dwd.de

Technical Officer: Michael Eisinger

European Space Agency Michael.Eisinger@esa.int

Document authors: Andrew T. Prata¹, Adam C. Povey^{1,2}, Roy G. Grainger^{1,2}, Simon R. Proud^{2,3}, & Martin Stengel⁴

- Atmospheric, Oceanic and Planetary Physics, University of Oxford, Oxford, OX1 3PU, UK
- National Centre for Earth Observation, Leicester, LE4 5SP, UK
- ³ RAL Space, STFC-RAL, Harwell Campus, Didcot, OX11 0QX, UK
- ⁴ Deutscher Wetterdienst, Offenbach am Main, Germany

E3UB

REF: E3UB

ISSUE: 1 Revision: 0 DATE: 27/3/2023

PAGE: 2

Contents

1	Unc	ertainty due to ancillary information	4
	1.1	Uncertainty due to surface emissivity	4
	1.2	Forward model sensitivity to surface emissivity uncertainty for ISCCP clouds	
	1.3	Uncertainty due to the temperature profiles	
	1.4	Uncertainty due to the specific humidity profiles	
2	Tota	al error budget for ancillary information	15
	2.1	Optically thin clouds	16
	2.2	Optically thick clouds	18
3	Sam	pling uncertainty	20
4	Imp	pact of varying spectral characteristics on cloud products	22



REF: E3UB ISSUE: 1 Revision: 0 DATE: 27/3/2023

PAGE: 3

Document Change Record

Document, Version	Date	Changes	Originator
E3UB Version 1.0	03/20/2023	Initial version	Andrew T. Prata, Adam C. Povey, Roy G. Grainger, Simon Proud, Martin Stengel
-	-	-	-

Purpose of this document

This document outlines the errors introduced to the products of Cloud_cci due to the use of ancillary data. Specifically, the effect of uncertainties in surface emissivity, temperature profiles and specific humidity profiles are quantified. The uncertainties in monthly mean cloud products introduced by the incomplete diurnal sampling of polar-orbiting sensors (e.g. SLSTR, AVHRR) are assessed. Finally, SLSTR and SEVIRI data are compared to assess the impact of using different spectral information on the resulting cloud products.

E3UB

REF: E3UB ISSUE: 1 Revision: 0 DATE: 27/3/2023

PAGE: 4

1 Uncertainty due to ancillary information

Here we describe a methodology to properly account for uncertainties associated with variables not included in the state vector (i.e. not directly retrieved) that are obtained from ancillary information. Within CC4CL, the error covariance matrix is defined by

$$\mathbf{S_y} = \mathbf{S}_{\text{noise}} + \mathbf{S}_{\text{pixel}} + \mathbf{S}_{\text{fm}},\tag{1}$$

where S_{noise} accounts for measurement noise, S_{pixel} accounts for uncertainty due to inadequacies in the planeparallel cloud assumption and imperfect co-registration and S_{fm} accounts for uncertainty in the forward model (we refer to these error terms collectively as non-ancillary parameter uncertainty hereafter). The CC4CL forward model requires ancillary information in order to compute top of the atmosphere radiance. To account for ancillary information uncertainty, we add a new error term to the error covariance matrix as follows

$$\mathbf{S_y} = \mathbf{S}_{\text{noise}} + \mathbf{S}_{\text{pixel}} + \mathbf{S}_{\text{fm}} + \mathbf{S}_{\text{anc}},\tag{2}$$

where S_{anc} accounts for uncertainty in ancillary information converted to measurement space. The main ancillary datasets included in CC4CL are the surface reflectance database from MODIS, the emissivity database (CAMEL) and the ERA5 meteorological database (profiles of temperature, specific humidity and ozone). Uncertainty in the surface reflectance, R_s , is presently accounted for in S_{fm} and we assume uncertainty in the ozone profiles is negligible compared to uncertainty in the temperature and humidity profiles, which leads us to define S_{anc} as follows

$$\mathbf{S}_{\mathrm{anc}} = \mathbf{S}_{\mathrm{anc},\epsilon_s} + \mathbf{S}_{\mathrm{anc},T} + \mathbf{S}_{\mathrm{anc},q},\tag{3}$$

where S_{anc,ϵ_s} , $S_{anc,T}$ and $S_{anc,q}$ represent the uncertainty in the surface emissivity database, ERA5 temperature profiles and ERA5 humidity profiles, respectively.

1.1 Uncertainty due to surface emissivity

To account for uncertainty due to the surface emissivity model parameter, the Jacobian matrix (\mathbf{K}_{ϵ_s}) must be derived so that uncertainty in the model parameter space, defined by the surface emissivity error covariance matrix, can be mapped into measurement space as follows

$$\mathbf{S}_{\mathrm{anc},\epsilon_s} = \mathbf{K}_{\epsilon_s} \mathbf{cov}(\delta \epsilon_s) \mathbf{K}_{\epsilon_s}^{\mathrm{T}}.$$
 (4)

The thermal channels used in the measurement vector within CC4CL are the 3.9, 11 and $12 \mu m$. If we consider the uncertainty associated with the surface emissivity for these channels then the surface emissivity error covariance matrix can be evaluated as

$$\mathbf{cov}(\delta\epsilon_s) = \begin{bmatrix} (\delta\epsilon_s(3.9\,\mu\text{m}))^2 & 0 & 0\\ 0 & (\delta\epsilon_s(11\,\mu\text{m}))^2 & 0\\ 0 & 0 & (\delta\epsilon_s(12\,\mu\text{m}))^2 \end{bmatrix},\tag{5}$$

where $\delta\epsilon_s(3.9~\mu\text{m})$, $\delta\epsilon_s(11~\mu\text{m})$ and $\delta\epsilon_s(12~\mu\text{m})$ are the surface emissivity uncertainties at 3.9, 11 and 12 μm , respectively. Here we assume that uncertainties in the surface emissivity for each channel are independent (i.e. off-diagonals are set to 0). Based on the work of Feltz et al. [2], we assume a surface emissivity uncertainties of 0.03, 0.01 and 0.01 for the 3.9 μm , 11 μm and 12 μm channels, respectively.

The Jacobian matrix, \mathbf{K}_{ϵ_s} , can be derived by taking the partial derivative of the thermal forward model with respect to the surface emissivity. The CC4CL forward model computes the top-of-the-atmosphere radiance, L_{TOA} as

$$L_{\text{TOA}} = L_{\text{ac}}^{\uparrow} + [L_{\text{ac}}^{\downarrow} R_{\text{db}}^{\uparrow}(\theta_v) + B(T_c)\epsilon(\theta_v) + L_{\text{bc}}^{\uparrow}(1 - \epsilon(\theta_v))]t_{\text{ac}}(\theta_v). \tag{6}$$



REF: E3UB

ISSUE: 1 Revision: 0 DATE: 27/3/2023

PAGE: 5

The Jacobian matrix is thus

$$\mathbf{K}_{\epsilon_{s}} = \begin{bmatrix} \frac{\partial L_{\text{TOA}}(3.9 \, \mu\text{m})}{\partial \epsilon_{s}(3.9 \, \mu\text{m})} & \frac{\partial L_{\text{TOA}}(3.9 \, \mu\text{m})}{\partial \epsilon_{s}(11 \, \mu\text{m})} & \frac{\partial L_{\text{TOA}}(3.9 \, \mu\text{m})}{\partial \epsilon_{s}(12 \, \mu\text{m})} \\ \frac{\partial L_{\text{TOA}}(11 \, \mu\text{m})}{\partial \epsilon_{s}(3.9 \, \mu\text{m})} & \frac{\partial L_{\text{TOA}}(11 \, \mu\text{m})}{\partial \epsilon_{s}(11 \, \mu\text{m})} & \frac{\partial L_{\text{TOA}}(11 \, \mu\text{m})}{\partial \epsilon_{s}(12 \, \mu\text{m})} \\ \frac{\partial L_{\text{TOA}}(12 \, \mu\text{m})}{\partial \epsilon_{s}(3.9 \, \mu\text{m})} & \frac{\partial L_{\text{TOA}}(12 \, \mu\text{m})}{\partial \epsilon_{s}(11 \, \mu\text{m})} & \frac{\partial L_{\text{TOA}}(12 \, \mu\text{m})}{\partial \epsilon_{s}(12 \, \mu\text{m})} \end{bmatrix} = \begin{bmatrix} \frac{\partial L_{\text{TOA}}(3.9 \, \mu\text{m})}{\partial \epsilon_{s}(3.9 \, \mu\text{m})} & 0 & 0 \\ 0 & \frac{\partial L_{\text{TOA}}(11 \, \mu\text{m})}{\partial \epsilon_{s}(11 \, \mu\text{m})} & 0 \\ 0 & 0 & \frac{\partial L_{\text{TOA}}(12 \, \mu\text{m})}{\partial \epsilon_{s}(12 \, \mu\text{m})} \end{bmatrix}, (7)$$

where, for a diagonal element in \mathbf{K}_{ϵ_s} ,

$$\frac{\partial L_{\text{TOA}}}{\partial \epsilon_s} = \frac{\partial L_{\text{bc}}^{\uparrow}}{\partial \epsilon_s} (1 - \epsilon) t_{\text{ac}}.$$
 (8)

Since L_{bc}^{\uparrow} is computed as a pre-processing task and depends on T_s , which is included in the state vector, it must be updated during the retrieval process. L_{bc}^{\uparrow} is computed as

$$L_{\rm bc}^{\uparrow} = L_{\rm bc,a}^{\uparrow} + (T_{\rm s} - T_{\rm s,a}) \frac{\partial B(T_{\rm s,a})}{\partial T_{\rm s,a}} \epsilon_s t_{\rm bc}. \tag{9}$$

Differentiating with respect to ϵ_s we have

$$\frac{\partial L_{bc}^{\uparrow}}{\partial \epsilon_s} = B(T_{s,a})t_{bc} + (T_s - T_{s,a})\frac{\partial B(T_{s,a})}{\partial T_{s,a}}t_{bc},\tag{10}$$

which gives us the partial derivative of the forward model with respect to surface emissivity as follows

$$\frac{\partial L_{\text{TOA}}}{\partial \epsilon_s} = \left[B(T_{\text{s,a}}) + (T_{\text{s}} - T_{\text{s,a}}) \frac{\partial B(T_{\text{s,a}})}{\partial T_{\text{s,a}}} \right] (1 - \epsilon) t_{\text{bc}} t_{\text{ac}}. \tag{11}$$

Finally, the uncertainty due to surface emissivity can be propagated through the forward model and converted to measurement space by evaluating the $\mathbf{K}_{\epsilon_s}\mathbf{cov}(\delta\epsilon_s)\mathbf{K}_{\epsilon_s}^{\mathrm{T}}$ matrix. For a particular diagonal element, we may write

$$\mathbf{S}_{\mathrm{anc},\epsilon_s}(i,i) = \mathbf{K}_{\epsilon_s} \mathbf{cov}(\delta \epsilon_s) \mathbf{K}_{\epsilon_s}^{\mathrm{T}}(i,i) = \left(\left[B(T_{\mathrm{s,a}}) + (T_{\mathrm{s}} - T_{\mathrm{s,a}}) \frac{\partial B(T_{\mathrm{s,a}})}{\partial T_{\mathrm{s,a}}} \right] (1 - \epsilon) t_{\mathrm{bc}} t_{\mathrm{ac}} \right)^2 (\delta \epsilon_s)^2. \tag{12}$$

1.2 Forward model sensitivity to surface emissivity uncertainty for ISCCP clouds

To evaluate the impact of surface emissivity uncertainty on the forward model we have evaluated the error covariance matrix, $\mathbf{S}_{\mathrm{anc},\epsilon_s}$, for six representative cloud types based on the ISCCP definitions (Table 1). We then tested the sensitivity of the forward model uncertainty (in brightness temperature for each thermal channel) by varying the cloud effective radius and cloud optical thickness for each cloud type. For each sensitivity test, we held the surface temperature constant at $T_s=295.18$ K and the surface emissivity at $\epsilon_s=0.98$. The results for the six ISSCP cloud types are shown in Figs. 1–6. Note that ISCCP defines clouds warmer than 260 K as liquid clouds composed of spherical droplets with an effective radius of 10 μ m and colder clouds are defined as ice clouds composed of crystals with effective radius of 30 μ m. For liquid water clouds we use the Segelstein [3] look-up tables. For ice particles we use the Baum et al. [1] general habit mixture look-up tables.

The results show that the impact of uncertainty in the surface emissivity for thermal channel wavelengths on the forward model uncertainty is a function of the diffuse emissivity of the cloud, which is a function of optical depth and effective radius. The uncertainty in TOA brightness temperature is negligible (an order of magnitude or more lower than non-ancillary parameter uncertainty) for the stratus, altostratus (water and ice phase) and deep convection across the range of their expected optical depths (as defined by ISCCP). However, the impact of surface emissivity uncertainty does become significant (comparable to non-ancillary parameter uncertainty) for clouds with low optical depths (\sim 1) such as the cumulus and cirrus clouds which have typical optical depths that are semi-transparent at split-window channel wavelengths (i.e 11 and 12 µm). Table 2 summarises the absolute TOA uncertainty (converted to brightness temperature) when surface emissivity uncertainty is propagated through the forward model for the set of representative ISCCP clouds considered here.

E3UB

REF: E3UB ISSUE: 1 Revision: 0 DATE: 27/3/2023

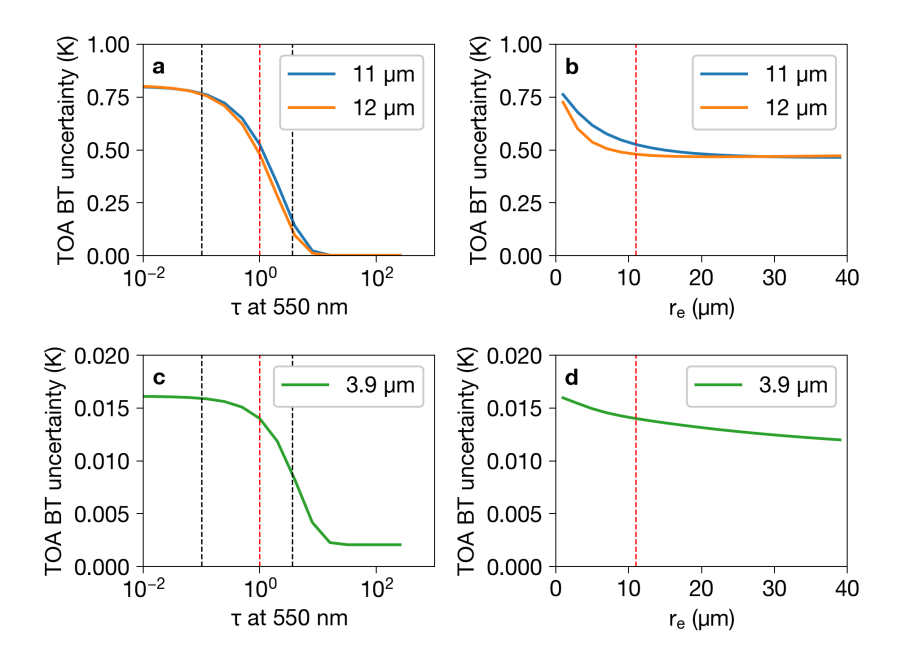


Figure 1: Impact of surface emissivity uncertainty on the CC4CL forward model for an ISCCP cumulus cloud (see Table 1 for assumed cloud properties). (a) Top-of-the-atmosphere (TOA) brightness temperature uncertainty in the 11 and 12 µm channels for the CC4CL forward model as a function of cloud optical thickness at 550 nm. (b) Same as (a) but as a function of effective radius. (c) and (d) are the same as (a) and (b) but for the 3.9 µm channel. The vertical black dashed lines indicate the ranges of optical depth that the particular cloud type is defined by according to ISCCP. The red dashed line indicates the state variable value that was held constant for the sensitivity tests.

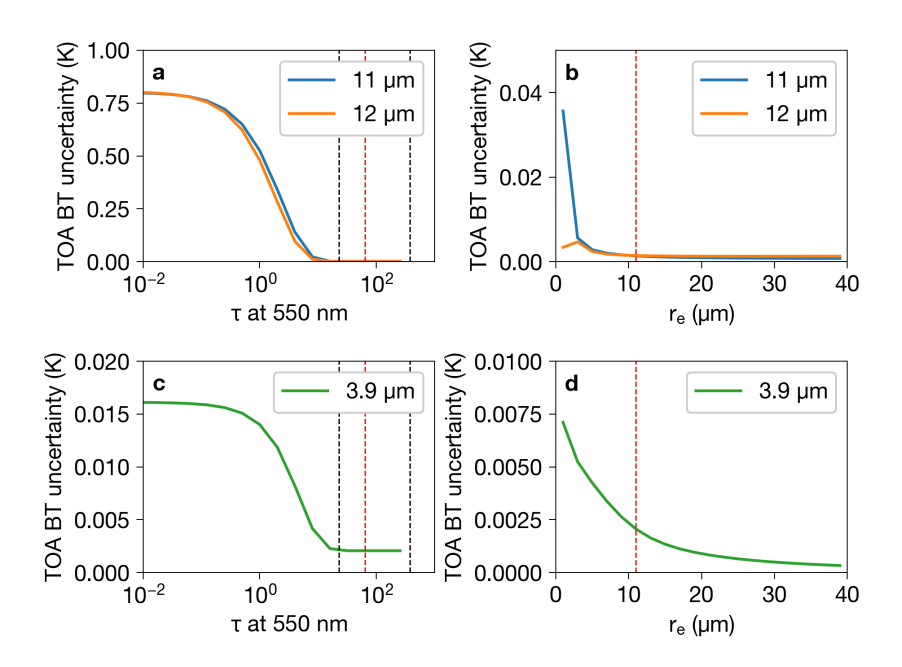


Figure 2: Same as Fig. 1 but for stratus.



REF: E3UB ISSUE: 1 Revision: 0 DATE: 27/3/2023

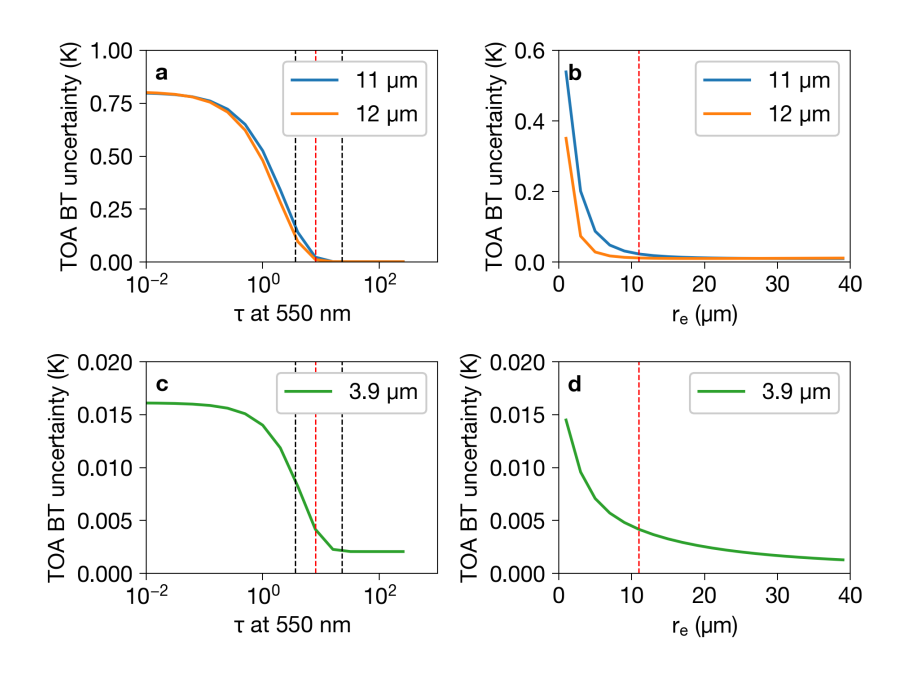


Figure 3: Same as Fig. 1 but for altostratus in the liquid water phase.

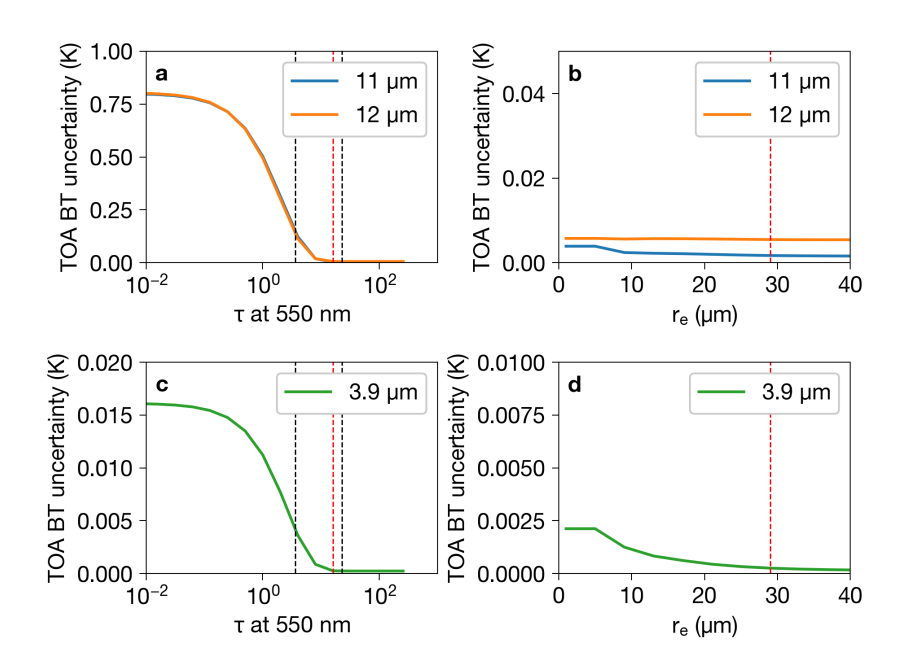


Figure 4: Same as Fig. 1 but for altostratus in the ice phase.

E3UB

REF: E3UB ISSUE: 1 Revision: 0 DATE: 27/3/2023

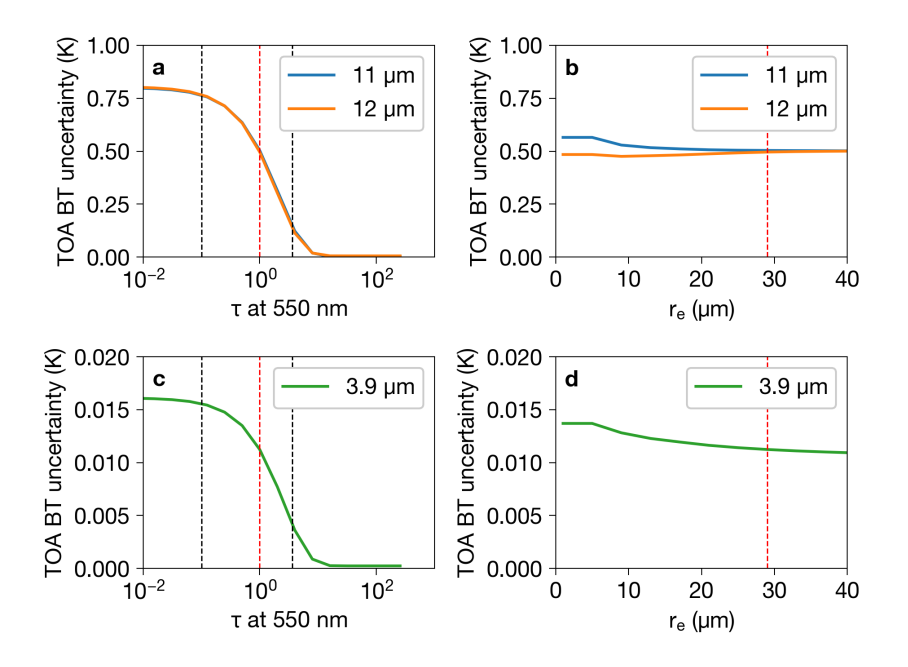


Figure 5: Same as Fig. 1 but for cirrus.

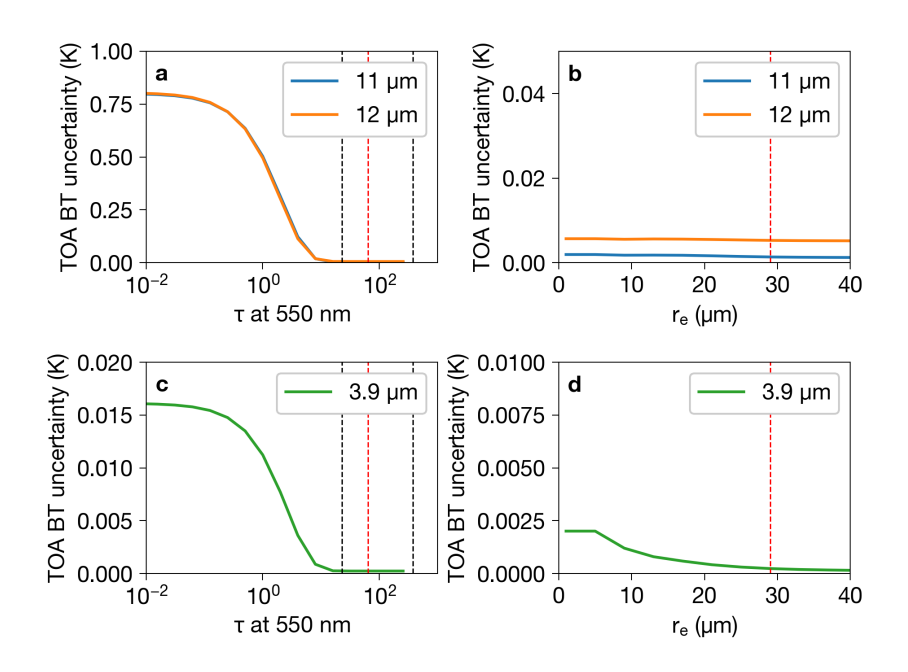


Figure 6: Same as Fig. 1 but for deep convection.



REF: E3UB

ISSUE: 1 Revision: 0 DATE: 27/3/2023

PAGE: 9

Table 1: Cloud types based on ISCCP definitions.

Cloud type	Cloud phase	r_e	$ au_{550\mathrm{nm}}$	p_c	T_c	h_c
Cumulus	Water	11 μm	1	810 hPa	288 K	2 km
Stratus	Water	11 µm	64	810 hPa	288 K	2 km
Altostratus	Water	11 µm	16	572 hPa	271 K	5 km
Altostratus	Ice	29 µm	16	453 hPa	258 K	7 km
Cirrus	Ice	29 µm	1	285 hPa	236 K	10 km
Deep convection	Ice	29 µm	64	285 hPa	236 K	10 km

Table 2: Absolute uncertainty for the TOA brightness temperature when surface emissivity uncertainty is propagated through the CC4CL forward model for six ISCCP cloud types.

1 0				J 1		
Channel	Cumulus	Stratus	Altostratus (water)	Altostratus (ice)	Cirrus	Deep convection
3.9 µm	0.0140 K	0.0021 K	0.0042 K	0.0003 K	0.0112 K	0.0002 K
11 μm	0.5258 K	0.0013 K	0.0228 K	0.0017 K	0.5034 K	0.0013 K
12 µm	0.4798 K	0.0014 K	0.0114 K	0.0055 K	0.4959 K	0.0053 K

1.3 Uncertainty due to the temperature profiles

To compute the forward model uncertainty (for a measurement vector of size m) due to uncertainty in ancillary a temperature profile with n levels, we follow the method proposed in Wang et al. [4], which recognises that uncertainty in the temperature profile can be mapped into forward model uncertainty by taking the partial derivative of the forward model with respect to the Planck radiance profile, B(T(p)), as follows

$$\mathbf{S}_{\text{anc},T} = \mathbf{K}_{\mathbf{L}_{\text{TOA}}/\mathbf{B}(\mathbf{T})} \mathbf{cov}(\delta \mathbf{B}(\mathbf{T})) \mathbf{K}_{\mathbf{L}_{\text{TOA}}/\mathbf{B}(\mathbf{T})}^{\mathrm{T}}, \tag{13}$$

where $\mathbf{K}_{\mathbf{L}_{TOA}/\mathbf{B}(\mathbf{T})}$ is an $m \times mn$ block diagonal matrix that represents the Jacobian of the forward model with respect to the Planck radiance profile, the covariance matrix representing the uncertainty in the Planck radiance profile is a $mn \times mn$ matrix given by

$$\mathbf{cov}(\delta \mathbf{B}(\mathbf{T})) = \mathbf{K}_{\mathbf{B}(\mathbf{T})/\mathbf{T}} \mathbf{cov}(\delta \mathbf{T}) \mathbf{K}_{\mathbf{B}(\mathbf{T})/\mathbf{T}}^{\mathrm{T}}, \tag{14}$$

where $\mathbf{K}_{\mathbf{B}(\mathbf{T})/\mathbf{T}}$ is an $mn \times n$ matrix (a vector of m, $n \times n$ sub-matrices) that represents the Jacobian of the Planck function with respect to the temperature profile and $\mathbf{cov}(\delta \mathbf{T})$ is the covariance matrix of the temperature profile, which is not diagonal.

To evaluate $\mathbf{cov}(\delta \mathbf{T})$, we first need a representation of uncertainty in the ERA5 ancillary temperature profiles. For this we use the ERA5 ensemble dataset which provides an ensemble consisting of 10 members. Figure 7(a) shows an example of the 10-member temperature profile ensemble over a single grid-box for 2 July 2019 at 15:00 UTC. The standard deviation of the temperature profiles is shown in Fig. 7(b). What is immediately apparent is that the ensemble spread grows with altitude, indicating that there is a larger uncertainty in the model's prediction of upper-atmospheric temperatures than in the lower-atmosphere (p > 100 hPa). There is also relatively large uncertainty at the location of the local inversion near $\sim 900 \text{ hPa}$.

The temperature profile covariance matrix can be computed as follows

$$\mathbf{cov}(\delta \mathbf{T}) = \begin{bmatrix} \delta T_1^2 & \cos(T_1, T_2) & \cdots & \cos(T_1, T_n) \\ \cos(T_2, T_1) & \delta T_2^2 & \cdots & \cos(T_2, T_n) \\ \vdots & \vdots & \ddots & \vdots \\ \cos(T_n, T_1) & \cos(T_n, T_2) & \cdots & \delta T_n^2 \end{bmatrix},$$
(15)



E3UB

REF: E3UB ISSUE: 1 Revision: 0 DATE: 27/3/2023

PAGE: 10

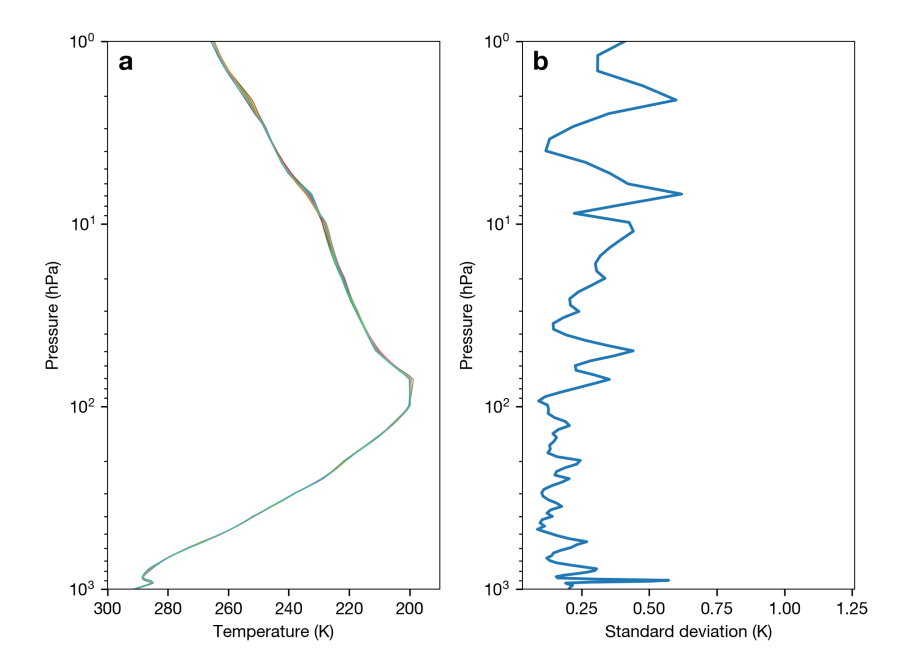


Figure 7: (a) ERA5 ensemble member temperature profiles for a grid-box located at 20°S, 5°W on 2 July 2016 at 15:00 UTC. (b) Standard deviation of the 10 ensemble member temperature profiles.

where $T_1 ldots T_n$ represent the temperature at each level in an atmospheric profile with n levels. Note that T_n is a vector of size 10 as we have 10 ensemble members. Figure 8 shows the covariance matrix of the temperature profile shown in Fig. 7. The covariances range from -0.56 K^2 to 1.45 K^2 and are largest along the diagonal of the matrix. The next step is to derive $K_{\mathbf{B}(\mathbf{T})/\mathbf{T}}$ which simply involves taking the partial derivative of the Planck function with respect to temperature. The matrix is constructed as follows

$$\mathbf{K}_{\mathbf{B}(\mathbf{T})/\mathbf{T}} = \begin{bmatrix} \mathbf{K}_{\mathbf{B}(3.9 \,\mu\text{m}, \mathbf{T})/\mathbf{T}} \\ \mathbf{K}_{\mathbf{B}(11 \,\mu\text{m}, \mathbf{T})/\mathbf{T}} \\ \mathbf{K}_{\mathbf{B}(12 \,\mu\text{m}, \mathbf{T})/\mathbf{T}} \end{bmatrix}. \tag{16}$$

Here $\mathbf{K_{B(T)/T}}$ is a matrix with m rows of $n \times n$ square matrices. For example, for the 3.9 μ m measurement, the $n \times n$ matrix would be computed as

$$\mathbf{K}_{\mathbf{B}(3.9 \, \mu m, \mathbf{T})/\mathbf{T}} = \begin{bmatrix} \frac{\partial B(3.9 \, \mu m, T_1)}{\partial T_1} & 0 & \cdots & 0 \\ 0 & \frac{\partial B(3.9 \, \mu m, T_2)}{\partial T_2} & \cdots & 0 \\ \vdots & \vdots & \ddots & \vdots \\ 0 & 0 & \cdots & \frac{\partial B(3.9 \, \mu m, T_n)}{\partial T_n} \end{bmatrix}.$$
(17)

This approach accounts for uncertainties in temperature at every level in the profile for each thermal infrared measurement.

With Eqs. 15 and 16 we can determine $\mathbf{cov}(\delta \mathbf{B}(\mathbf{T}))$. However, in order to propagate the uncertainty through the forward model we need to determine $\mathbf{K}_{\mathbf{L}_{TOA}/\mathbf{B}(\mathbf{T})}$, which is an $m \times mn$ block diagonal matrix represented as follows

$$\mathbf{K}_{\mathbf{L}_{\text{TOA}}/\mathbf{B}(\mathbf{T})} = \begin{bmatrix} \mathbf{K}_{L_{\text{TOA}}(3.9 \ \mu\text{m})/\mathbf{B}(\mathbf{T})} & 0 & 0\\ 0 & \mathbf{K}_{L_{\text{TOA}}(11 \ \mu\text{m})/\mathbf{B}(\mathbf{T})} & 0\\ 0 & 0 & \mathbf{K}_{L_{\text{TOA}}(12 \ \mu\text{m})/\mathbf{B}(\mathbf{T})} \end{bmatrix}, \tag{18}$$



REF: E3UB ISSUE: 1 Revision: 0 DATE: 27/3/2023

PAGE: 11

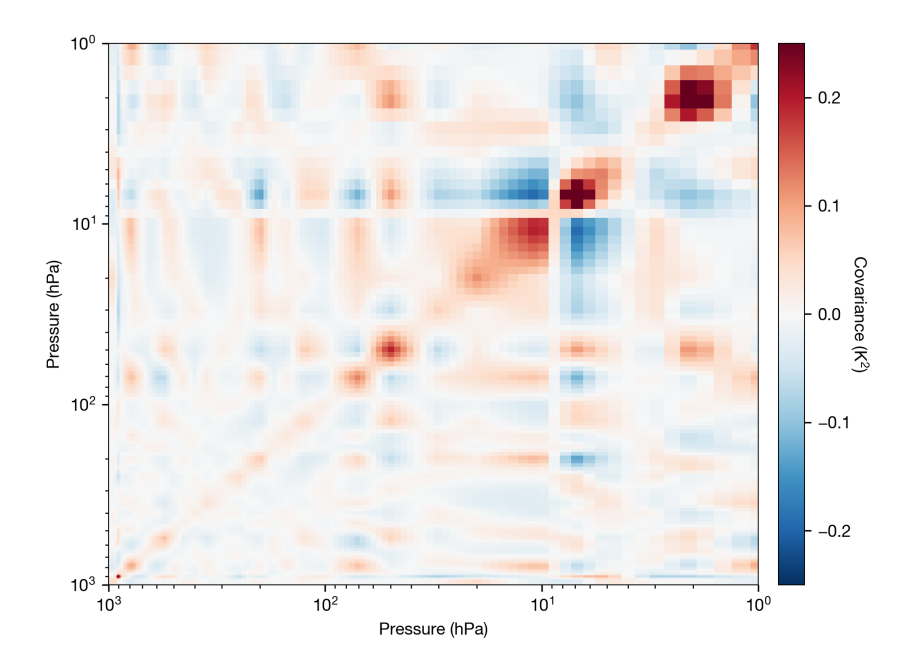


Figure 8: Temperature profile covariance matrix for the ERA5 ensemble profiles shown in Fig. 7.

where $\mathbf{K}_{L_{\text{TOA}}(3.9 \ \mu\text{m})/\mathbf{B}(\mathbf{T})}$, $\mathbf{K}_{L_{\text{TOA}}(11 \ \mu\text{m})/\mathbf{B}(\mathbf{T})}$ and $\mathbf{K}_{L_{\text{TOA}}(12 \ \mu\text{m})/\mathbf{B}(\mathbf{T})}$ are $1 \times n$ matrices, which can be derived by taking the partial derivative of the forward model with respect to the Planck radiance profile for the 3.9 μ m, 11 μ m and 12 μ m measurements, respectively. Recalling that the thermal forward model can be stated as

$$L_{\text{TOA}}(\lambda) = L_{\text{ac}}^{\uparrow} + [L_{\text{ac}}^{\downarrow} R_{\text{db}}^{\uparrow}(\theta_v) + B(T_c)\epsilon(\theta_v) + L_{\text{bc}}^{\uparrow}(1 - \epsilon(\theta_v))]t_{\text{ac}}(\theta_v)$$
(19)

and assuming the reflected portion of downward radiation above the cloud is negligible ($L_{\rm ac}^{\downarrow}R_{\rm db}^{\uparrow}(\theta_v)\approx 0$) then we have

$$L_{\text{TOA}}(\lambda) = \int_{p_c}^{0} B[T(p)]W(p)d\ln p + \epsilon B(T_c)t_{\text{ac}} + (1 - \epsilon)t_{\text{ac}} \left[\epsilon_s B(T_s)t_{\text{bc}} + \int_{p_s}^{p_c} B[T(p)]W(p)d\ln p\right], \quad (20)$$

where we have written the upward, above and below cloud radiances in terms of the Planck function; $W(p) = \partial t(p)/\partial \ln p$, is the weighting function of the channel and angular and wavelength dependencies on the right-hand side of the equation are implied. Differentiating with respect to the Planck radiance profile, B[T(p)], we have

$$\mathbf{K}_{L_{\text{TOA}}(\lambda)/\mathbf{B}(\mathbf{T})} = \frac{\partial}{\partial B[T(p)]} \left(\int_{p_c}^{0} B[T(p)]W(p)d\ln p \right) + \frac{\partial}{\partial B[T(p)]} \left((1 - \epsilon)t_{\text{ac}} \int_{p_s}^{p_c} B[T(p)]W(p)d\ln p \right). \tag{21}$$

Applying the Leibniz integral rule and after some algebraic manipulation we arrive at an analytical solution for the Jacobians

$$\mathbf{K}_{L_{\text{TOA}(\lambda)}/\mathbf{B}(\mathbf{T})} = (1 - t_{\text{ac}}) + (1 - \epsilon)t_{\text{ac}}(t_{\text{ac}} - t_{\text{ac}}t_{\text{bc}}). \tag{22}$$

As we found for the impact of surface emissivity uncertainty on the TOA radiance, the degree to which uncertainty in the temperature profile impacts the forward model uncertainty depends on the cloud properties contained in ϵ above. Tables 3–8 show the covariance matrix, $\mathbf{S}_{\text{anc},T}$, that results from using the ERA5, 10-member temperature profile ensemble to represent temperature profile uncertainty for each of the six ISCCP

E3UB

REF: E3UB ISSUE: 1 Revision: 0 DATE: 27/3/2023

PAGE: 12

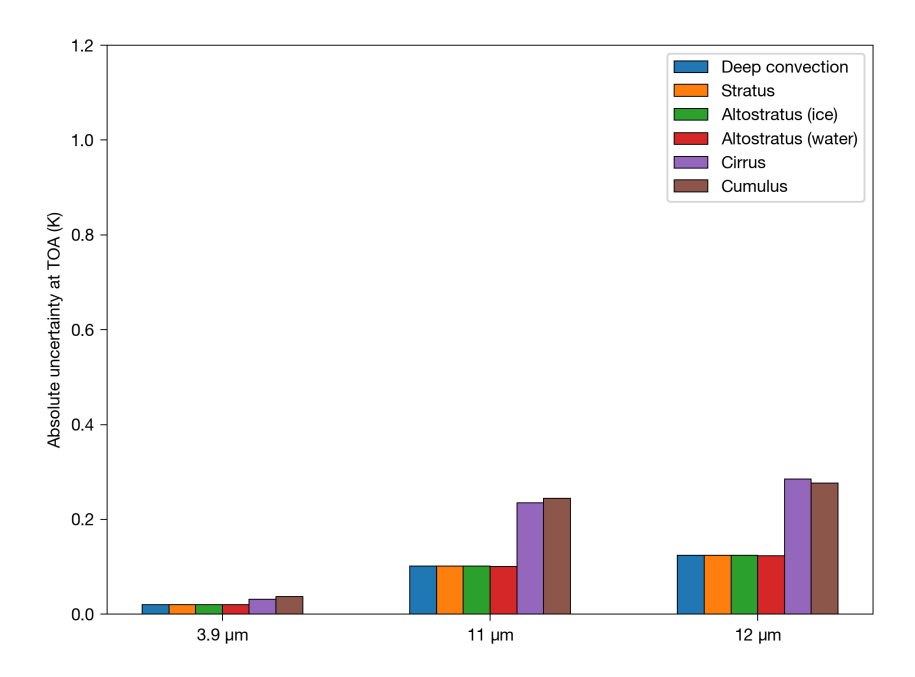


Figure 9: Top-of-atmosphere (TOA) brightness temperature uncertainty in the CC4CL forward model due to uncertainty in the ERA5 temperature profiles. Uncertainties are computed as the square root of the variances along the diagonal of the covariance matrices computed for each cloud type. Note that the covariance matrices are not diagonal.

cloud types specified in Table 1. Figure 9 shows the square root of the variance (in K) along the diagonal of the covariance matrix for each cloud type and thermal infrared measurement channel.

The results are interesting as the uncertainties for the cumulus and cirrus cloud types for the 11 and 12 μ m channels are comparable to non-ancillary parameter uncertainty in those channels. Thus incorporation of uncertainty due to temperature profile uncertainty may have a non-negligible impact on the retrieved state for the CC4CL cloud retrieval. However, this impact will most likely only affect the cloud-top height retrieval as the information on particle size and optical depth of the cloud mainly derives from the near-infrared and visible reflectance measurements. In addition, the representation of uncertainty in the temperature profile is probably overestimated as the meteorological dataset used in the forward model is the assimilated meteorological data which has been optimised to fit *in situ* measurements which will have a smaller uncertainty compared to ensemble model variances.

Table 3: Error covariance matrix representing the uncertainty in the forward model due to uncertainty in the temperature profile for an ISCCP cumulus cloud. Elements of the matrix are in units of K^2 .

	3.9 μm	11 µm	12 µm
3.9 µm	0.0014	0.0089	0.0101
11 μm	0.0089	0.0596	0.0675
12 µm	0.0101	0.0675	0.0766



REF: E3UB ISSUE: 1 Revision: 0

DATE: 27/3/2023 PAGE: 13

Table 4: Same as Table 3 but for stratus.

	3.9 µm	11 µm	12 µm
3.9 µm	0.0004	0.0018	0.0022
11 μm	0.0018	0.0103	0.0127
12 μm	0.0022	0.0127	0.0155

Table 5: Same as Table 3 but for altocumulus in the liquid water phase.

	3.9 µm	11 µm	12 µm
3.9 µm	0.0004	0.0018	0.0021
11 μm	0.0018	0.0101	0.0124
12 µm	0.0021	0.0124	0.0153

1.4 Uncertainty due to the specific humidity profiles

To determine uncertainties in the forward model related to uncertainties in the ERA5 specific humidity profile, q(p), we adopt a numerical approach. The error covariance matrix for the specific humidity profile can be written as follows

$$\mathbf{S}_{\text{anc},q} = \mathbf{K}_{\mathbf{L}_{\text{TOA}}/\mathbf{q}} \mathbf{cov}(\delta \mathbf{q}) \mathbf{K}_{\mathbf{L}_{\text{TOA}}/\mathbf{q}}^{\text{T}}, \tag{23}$$

where $\mathbf{cov}(\delta\mathbf{q})$ is an $n\times n$ and is computed in the same way as the $\mathbf{cov}(\delta\mathbf{T})$ above using the ERA5 ensemble dataset and $\mathbf{K}_{\mathbf{L}_{TOA}/\mathbf{q}}$ is the Jacobian of the forward model with respect to the specific humidity profile. Figure 10(a) shows the 10-member ensemble of specific humidity profiles and the standard deviation of these profiles is shown in Fig. 10(b). The y-axis is only shown up to 200 hPa because the water vapour concentrations go to zero at higher altitudes. The largest spread in the ensemble occurs near the local inversion as was found for the temperature profile ensemble; however, the model spread does not grow with altitude in contrast to the temperature profile ensemble. The relative uncertainty (computed as the ensemble standard deviation divided by the mean) is larger that 20 % at some altitudes, but varies mostly between 5–15 % (Fig. 10(c)).

The specific humidity covariance matrix $(\mathbf{cov}(\delta \mathbf{q}))$ is shown in Fig. 11. The specific humidity covariances range from -0.04 $(g/kg)^2$ to 0.55 $(g/kg)^2$ with the highest values along the diagonal of the matrix (maximum occurring at the local inversion).

The specific humidity Jacobians are expressed as an $m \times n$ matrix as follows

$$\mathbf{K}_{\mathbf{L}_{\text{TOA}}/\mathbf{q}} = \begin{bmatrix} \mathbf{K}_{L_{\text{TOA}}(3.9 \ \mu\text{m})/\mathbf{q}} \\ \mathbf{K}_{L_{\text{TOA}}(11 \ \mu\text{m})/\mathbf{q}} \\ \mathbf{K}_{L_{\text{TOA}}(12 \ \mu\text{m})/\mathbf{q}} \end{bmatrix}, \tag{24}$$

where, each channel/wavelength is represented by a vector consisting of n elements (or a $1 \times n$ matrix). For the measurement vector used within CC4CL they are

$$\mathbf{K}_{L_{\text{TOA}}(3.9 \ \mu\text{m})/\mathbf{q}} = \left[\frac{\partial L_{\text{TOA}}(3.9 \ \mu\text{m})}{\partial q_1}, \frac{\partial L_{\text{TOA}}(3.9 \ \mu\text{m})}{\partial q_2}, \cdots, \frac{\partial L_{\text{TOA}}(3.9 \ \mu\text{m})}{\partial q_i}, \cdots, \frac{\partial L_{\text{TOA}}(3.9 \ \mu\text{m})}{\partial q_n} \right], \quad (25)$$

$$\mathbf{K}_{L_{\text{TOA}}(11 \ \mu\text{m})/\mathbf{q}} = \left[\frac{\partial L_{\text{TOA}}(11 \ \mu\text{m})}{\partial q_1}, \frac{\partial L_{\text{TOA}}(11 \ \mu\text{m})}{\partial q_2}, \cdots, \frac{\partial L_{\text{TOA}}(11 \ \mu\text{m})}{\partial q_j}, \cdots, \frac{\partial L_{\text{TOA}}(11 \ \mu\text{m})}{\partial q_n} \right]$$
(26)

and

$$\mathbf{K}_{L_{\text{TOA}}(12 \, \mu\text{m})/\mathbf{q}} = \left[\frac{\partial L_{\text{TOA}}(12 \, \mu\text{m})}{\partial q_1}, \frac{\partial L_{\text{TOA}}(12 \, \mu\text{m})}{\partial q_2}, \cdots, \frac{\partial L_{\text{TOA}}(12 \, \mu\text{m})}{\partial q_j}, \cdots, \frac{\partial L_{\text{TOA}}(12 \, \mu\text{m})}{\partial q_n} \right]. \quad (27)$$



E3UB

REF: E3UB ISSUE: 1 Revision: 0 DATE: 27/3/2023

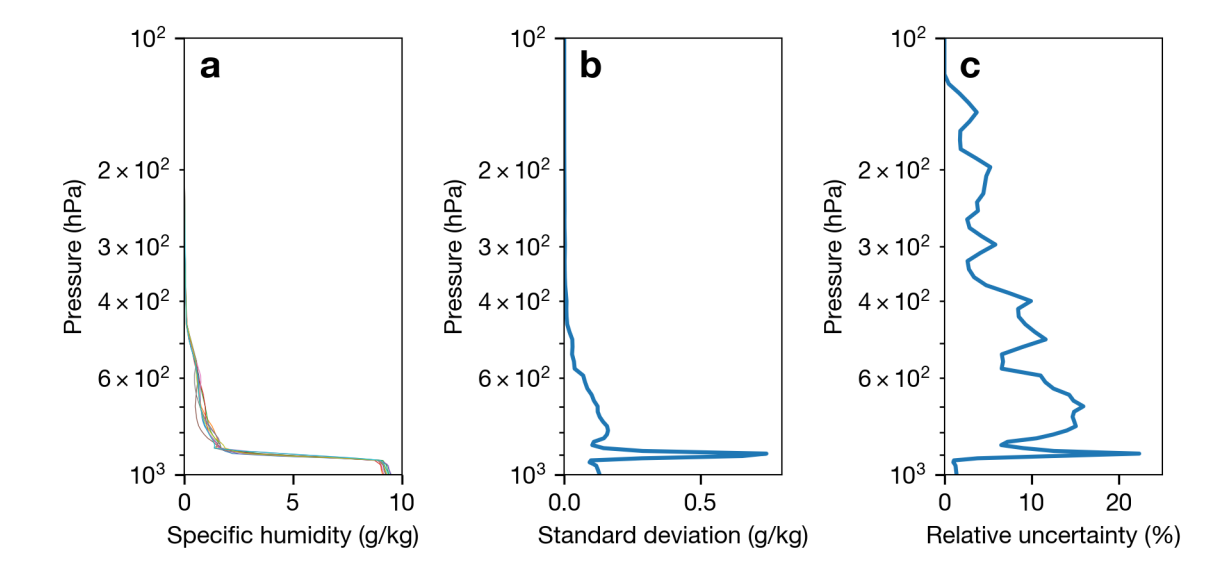


Figure 10: (a) ERA5 ensemble member specific humidity profiles for a grid-box located at 20°S, 5°W on 2 July 2016 at 15:00 UTC. (b) Standard deviation of the 10 ensemble member specific humidity profiles. (c) Relative uncertainty computed as the standard deviation divided by the ensemble mean.

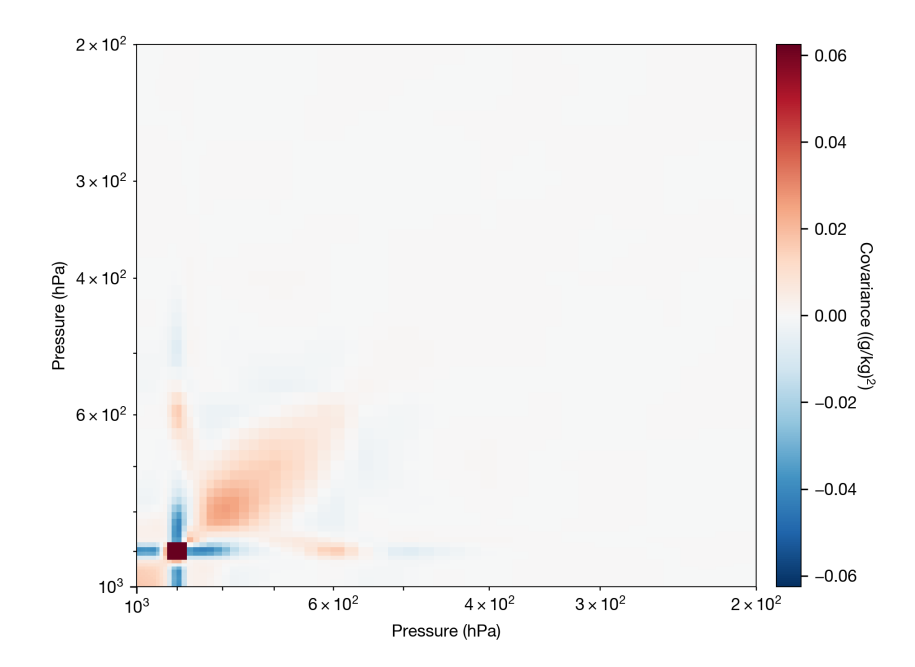


Figure 11: Specific humidity profile covariance matrix for the ERA5 ensemble profiles shown in Fig. 10(a).



REF: E3UB ISSUE: 1 Revision: 0

DATE: 27/3/2023 PAGE: 15

Table 6: Same as Table 3 but for altocumulus in the ice phase.

	3.9 µm	11 µm	12 µm
3.9 µm	0.0004	0.0019	0.0023
11 μm	0.0019	0.0103	0.0126
12 µm	0.0023	0.0126	0.0154

Table 7: Same as Table 3 but for cirrus.

	3.9 µm	11 µm	12 µm
	0.0010	0.0072	0.0088
11 μm	0.0072	0.0551	0.0669
12 μm	0.0088	0.0669	0.0812

To numerically determine the partial derivatives of the forward model with respect to the specific humidity profile for each measurement, we perturbed the ERA5 specific humidity profile by 5 %. The rate of change in TOA radiance due to a small change in the specific humidity profile is then computed as

$$\frac{\partial L_{\text{TOA}}(\lambda)}{\partial q_j} = \frac{L_{\text{TOA}}^{\lambda}(q_j + \Delta q_j) - L_{\text{TOA}}^{\lambda}(q_j)}{\Delta q_j},\tag{28}$$

where j represents the level in the atmosphere where the cloud is placed and $\Delta q_i = 0.05 \times q_i$.

Figure 12 shows the square root of the variance (in K) along the diagonal of the covariance matrix, $S_{anc,q}$, for the six ISCCP cloud types as before (see Table 1) and Tables 9–14 show the corresponding covariance matrices. As was found for the temperature profile and surface emissivity profiles, the uncertainty is dependent upon the cloud properties with the highest uncertainties corresponding to the clouds defined with the lowest optical depths (i.e. cumulus and cirrus). The uncertainty due to uncertainty in the specific humidity profiles is highest for the 12 µm channel. For the cirrus and cumulus clouds, uncertainty in the 12 µm channel approaches 1 K (larger than non-ancillary parameter uncertainty) but for all other cloud types the 12 µm channel uncertainty is ~ 0.30 K. The influence of specific humidity uncertainty on the 12 µm channel is not surprising as this channel is most affected by water vapour compared to the 3.9 µm and 11 µm channels studied here. The impact of uncertainty in the specific humidity profiles would be expected to be even higher for measurements more strongly responding to water vapour (e.g. 6.25 µm and 7.35 µm). Thus if water vapour channels are to be used in the measurement vector in the future, emphasis on reducing or better characterising water vapour uncertainty is recommended. Another approach would be to use channels that are less affected by water vapour such as the 10.5 µm channel available from the Flexible Combined Imager aboard the recently launched MTG-II satellite.

2 Total error budget for ancillary information

Figure 13 shows the error budget for all ancillary error terms ($\mathbf{S}_{\mathrm{anc},\epsilon_s}$, $\mathbf{S}_{\mathrm{anc},T}$, $\mathbf{S}_{\mathrm{anc},q}$ and $\mathbf{S}_{\mathrm{anc}}$) for each of the six ISCCP cloud types considered in the present work. For comparison, we have also plotted (black dots) uncertainties currently assumed for each thermal channel that account for non-ancillary parameter uncertainty, uncertainties associated with co-registration and scene homogeneity, and forward model uncertainty. The results of the error budget reveal clear differences in the forward model uncertainty sensitivity between the optically thin ($\tau_{550~\mathrm{nm}} \sim 1$) and thick ($\tau_{550~\mathrm{nm}} \sim 16$ –64) cloud types.



E3UB

REF: E3UB ISSUE: 1 Revision: 0 DATE: 27/3/2023

PAGE: 16

Table 8: Same as Table 3 but for deep convection.

	3.9 µm	11 µm	12 µm
3.9 µm	0.0004	0.0019	0.0023
11 µm	0.0019	0.0103	0.0126
12 µm	0.0023	0.0126	0.0154

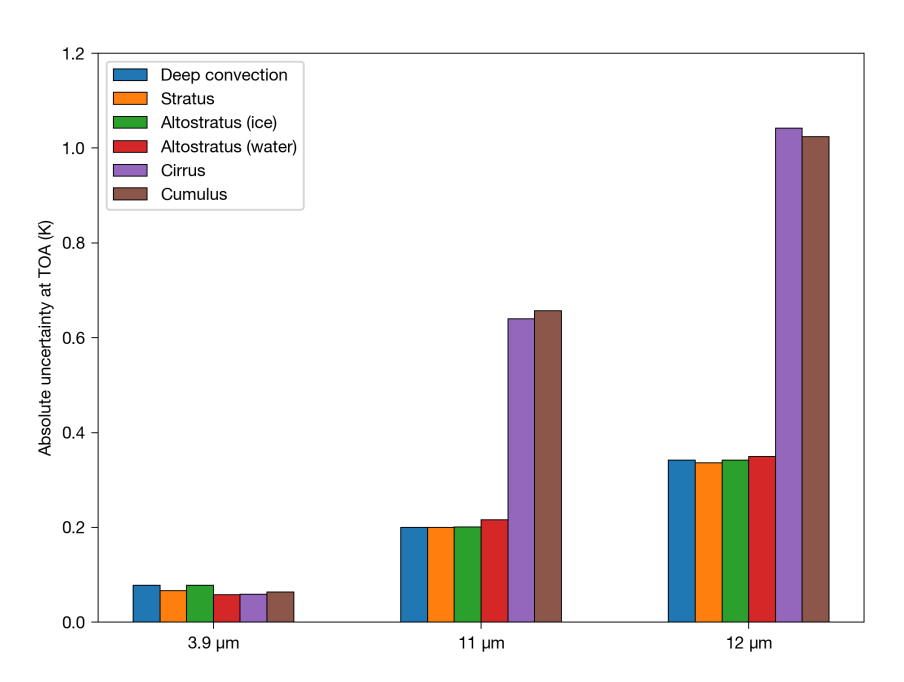


Figure 12: Top-of-atmosphere (TOA) brightness temperature uncertainty in the CC4CL forward model due to uncertainty in the ERA5 specific humidity profiles. Uncertainties are computed as the square root of the variances along the diagonal of the covariance matrices computed for each cloud type. Note that the covariance matrices are not diagonal.

2.1 Optically thin clouds

Uncertainties in the forward model due to ancillary information are highest for optically thin clouds ($\tau_{550\,\mathrm{nm}} \sim 1$), represented here by cumulus and cirrus. It is important to note that the terms 'cumulus' and 'cirrus' were defined based on the ISCCP standards and that *real* cumulus and cirrus clouds might not fit this terminology. The results of the error budget indicate that the optical depth of the cloud controls the degree to which uncertainty in ancillary information influences the forward model uncertainty. Interestingly, the impact of modifying the effective radius, cloud phase and cloud-top pressure on the total uncertainty budget is small compared to changes in the optical depth of the cloud. This can be understood by comparing the covariance matrices for cumulus cloud (liquid water, $r_e=11~\mu\mathrm{m},\,p_c=810~\mathrm{hPa}$) with the covariance matrices for cirrus cloud (ice, $r_e=29~\mu\mathrm{m},\,p_c=285~\mathrm{hPa}$). The covariance matrices for both cloud types are very similar, despite the cloud phase, effective radius and cloud-top pressure all being different; the only cloud parameter they have in common is the optical depth.

The ancillary parameter with the smallest contribution to the total error budget for the optically thin clouds is the temperature profile. Essentially, for optically thin clouds, the surface emissivity uncertainty becomes important along with tropospheric water vapour (represented by the specific humidity profiles). For the 11 μ m channel, the uncertainties due to the surface emissivity and specific humidity profile are comparable but for the 12 μ m channel, the specific humidity uncertainty dominates the error budget due to the largest absorption of



REF: E3UB ISSUE: 1 Revision: 0 DATE: 27/3/2023

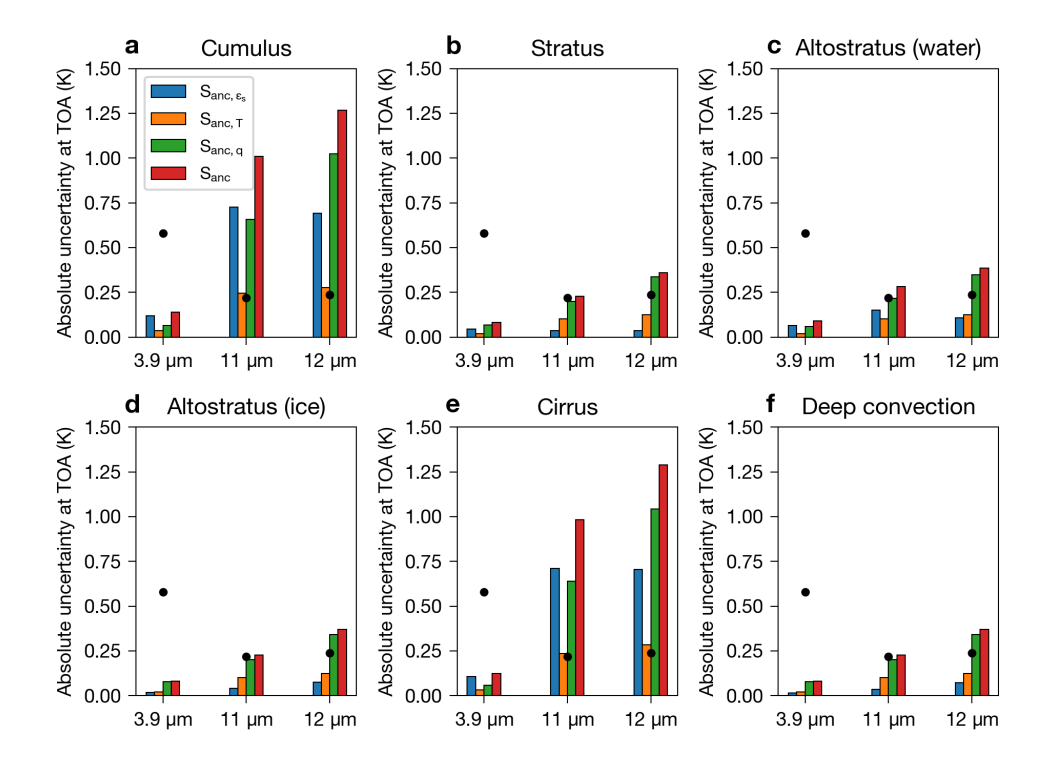


Figure 13: Error budget accounting for uncertainties in ancillary information for (a) Cumulus, (b) Stratus, (c) Altostratus in the liquid water phase, (d) Altostratus in the ice phase, (e) Cirrus and (f) Deep convection. See Table 1 for ISCCP cloud definitions. Note that the values shown represent the square root of the diagonal of the error covariance matrices. Black dots indicate currently assumed non-ancillary parameter uncertainty (in K).



E3UB

REF: E3UB ISSUE: 1 Revision: 0 DATE: 27/3/2023

PAGE: 18

Table 9: Error covariance matrix representing the uncertainty in the forward model due to uncertainty in the specific humidity profile for an ISCCP cumulus cloud. Elements of the matrix are in units of K^2 .

	3.9 µm	11 µm	12 μm
3.9 µm	0.0041	0.0421	0.0655
11 μm	0.0421	0.4319	0.6728
12 μm	0.0655	0.6728	1.0484

Table 10: Same as Table 9 but for stratus.

	3.9 µm	11 µm	12 µm
3.9 µm	0.0044	0.0100	0.0146
11 µm	0.0100	0.0401	0.0661
12 µm	0.0146	0.0661	0.1131

water vapour in this band compared with the other thermal channels. For both cumulus and cirrus, the absolute brightness temperature uncertainty at TOA for the 11 μm and 12 μm channels outweigh the uncertainty found for the 3.9 μm channel. For the 3.9 μm , the total ancillary parameter uncertainty (0.13 K) is approximately one fifth of the currently assumed non-ancillary parameter uncertainty in this channel (0.58 K; Fig.13(a) and (b), black dots). For the 11 μm and 12 μm channels, the total ancillary parameter uncertainties (1 K for 11 μm and 1.3 K for 12 μm) are significantly higher than the currently assumed non-ancillary parameter uncertainty in these channels (0.22 K for 11 μm and 0.24 K for 12 μm ; Fig.13(a) and (b), black dots).

2.2 Optically thick clouds

For the optically thick clouds (stratus, altostratus water, altostratus ice and deep convection), uncertainties due to surface emissivity and the temperature profile are small compared to non-ancillary parameter uncertainty for all thermal channels. Overall, the total absolute brightness temperature uncertainty in the 3.9 μm ($\sim\!0.08$ K) is much smaller than the currently assumed non-ancillary parameter uncertainty (0.58 K). For the 11 μm and 12 μm channels, however, the absolute TOA brightness temperature uncertainty due to ancillary parameter uncertainty (0.23 K for 11 μm and 0.36 K for 12 μm) is comparable to the non-ancillary parameter uncertainty currently assumed for these channels (0.22 K for 11 μm and 0.24 K for 12 μm), despite the high optical depth of the clouds ($\tau_{550\,nm}$ from 16–64). This is because the uncertainty budget for the 11 μm and 12 μm channels is dominated by uncertainty in the specific humidity profiles. It is important to note that the specific humidity uncertainty assumed here is derived from the ERA5 ensemble product and, as with the temperature profile uncertainty, is a conservative estimate. Regardless, the method proposed here is flexible and it is straightforward to re-compute the error budget when more precise estimates of temperature and specific humidity profiles become available.



REF: E3UB

ISSUE: 1 Revision: 0 DATE: 27/3/2023

Table 11: Same as Table 9 but for altocumulus in the liquid water phase.

	3.9 µm	11 µm	12 µm
3.9 µm	0.0034	0.0105	0.0155
11 μm	0.0105	0.0468	0.0748
12 µm	0.0155	0.0748	0.1219

Table 12: Same as Table 9 but for altocumulus in the ice phase.

	3.9 µm	11 µm	12 µm
3.9 µm	0.0061	0.0098	0.0128
11 μm	0.0098	0.0402	0.0670
12 μm	0.0128	0.0670	0.1167

Table 13: Same as Table 9 but for cirrus.

	3.9 µm	11 µm	12 μm
3.9 µm	0.0035	0.0370	0.0600
11 μm	0.0370	0.4099	0.6671
12 µm	0.0600	0.6671	1.0859

Table 14: Same as Table 3 but for deep convection.

	3.9 µm	11 µm	12 μm
3.9 µm	0.0061	0.0097	0.0127
11 µm	0.0097	0.0401	0.0669
12 µm	0.0127	0.0669	0.1168

E3UB

REF: E3UB ISSUE: 1 Revision: 0 DATE: 27/3/2023

PAGE: 20

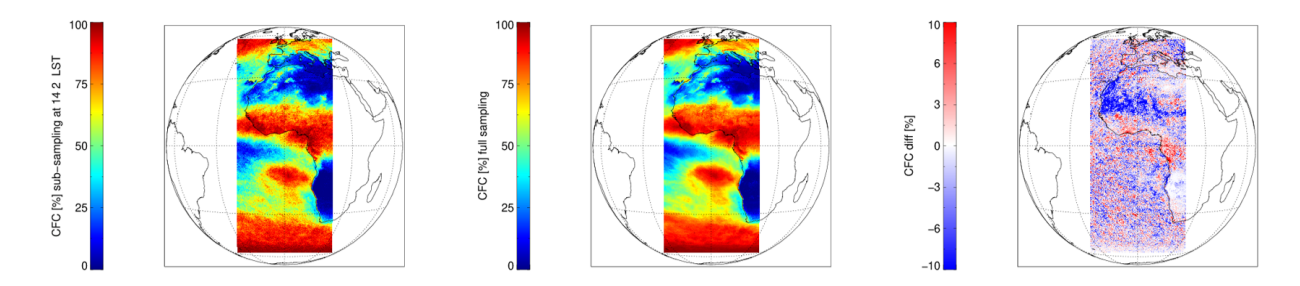


Figure 14: Left: monthly mean cloud fraction from SEVIRI observations, but sampled at 2 PM local solar time - emulating the monthly mean derived from a polar-orbiting satellite with overpass time at 2 PM. Middle: monthly mean cloud fraction from SEVIRI observations using all available observations. Right: difference between subsampled and full sampling monthly means.

3 Sampling uncertainty

Temporally highly resolved, geostationary observations were utilized to analyse the potential systematic errors introduced by reduced, and thus potentially imperfect, diurnal sampling of polar-orbiting sensors (e.g. SLSTR). It is worth noting that this analysis benefits from the fact that the same cloud retrieval scheme has been used for SEVIRI and for SLSTR (and other polar-orbiting sensors) in Cloud_cci. This reduces the risk of falsely attributing results in this study.

The reduced temporal sampling was emulated by temporally sub-sampling the CLAAS-3 data (at specific local solar times) and comparing to the fully sampled CLAAS-3 data. Figure 14 shows cloud fraction maps for reduced and full sampling alongside their difference. Although systematic deviations might exist locally, over a larger domain these seem to average out. Figures 15 (morning orbits) and 16 (afternoon orbits) show frequency distributions over the mean differences of all pixels in the domain indicated in Figure 14 for all main cloud variables for varying sampling scenarios (observations times). Relatively speaking, the reduced temporal sampling — twice per day for CFC, CTP and CPH and once per day for COT, LWP and IWP — does not introduce severe systematic uncertainties when considered over a larger domain. Furthermore, the biases remain small as observation time is varied. For CFC the bias is most positive around midday. CTP and CPH show a similarly less negative / more positive at midday compared to morning and afternoon. The bias for COT remains relatively small throughout the day, with a decrease around midday. For LWP, the bias becomes more negative through the day, while the opposite is observed for IWP. A slight exception is CTP, for which an increasingly positive bias is seen towards midday, decreasing thereafter. The numbers presented in Figures 15 and 16 also enable a basic quantification of theoretical trends in the any time series analysis caused by orbital drift, i.e. when the orbit and thus the local observation times do not remain stable over time.

- 1. Assuming an overpass time of 10:00 and a drift of the overpass time to 11:00 within 5 years, the 5-year trends introduced by this drift amount to: -0.2% for CFC, +4.3 hPa for CTP, +1.35% for liquid cloud fraction (CPH), -0.2 for COT, -0.68 g/m-2 for LWP and 0 g/m-2 for IWP.
- 2. Assuming an overpass time of 14:00 and a drift of the overpass time to 15:00 within 5 years, the 5-year trends introduced by this drift amount to: +0.9% for CFC, -1.7 hPa for CTP, -1.64% for liquid cloud fraction (CPH), +0.1 for COT, -1.08 g/m-2 for LWP and +0.77 g/m-2 for IWP.



REF: E3UB ISSUE: 1 Revision: 0

DATE: 27/3/2023 PAGE: 21

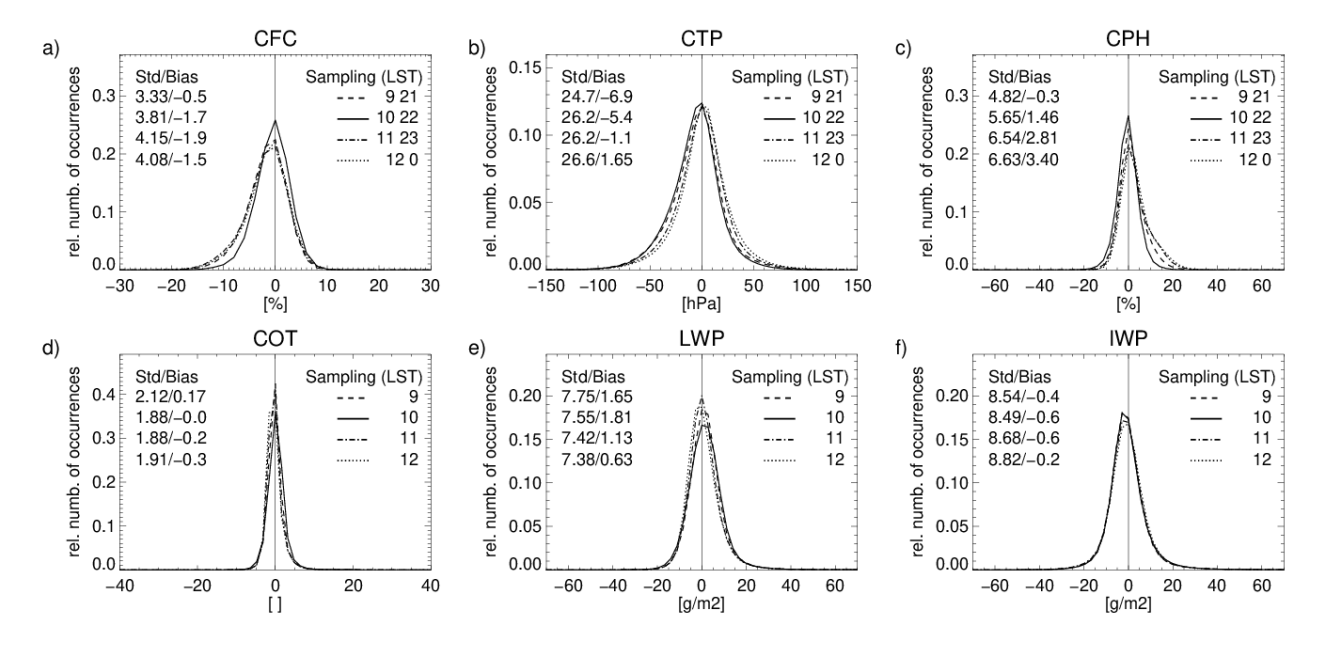


Figure 15: Sampling uncertainty for polar-orbiting sensors for morning overpasses at 9:00, 10:00, 11:00, 12:00 local solar time. Statistics are derived from temporally subsampling geostationary (SEVIRI) 15min data. For CFC, CTP and CPH the sampling is done twice as day (ascending and descending node), while for COT, LWP and IWP the data shown only includey daylight overpasses.

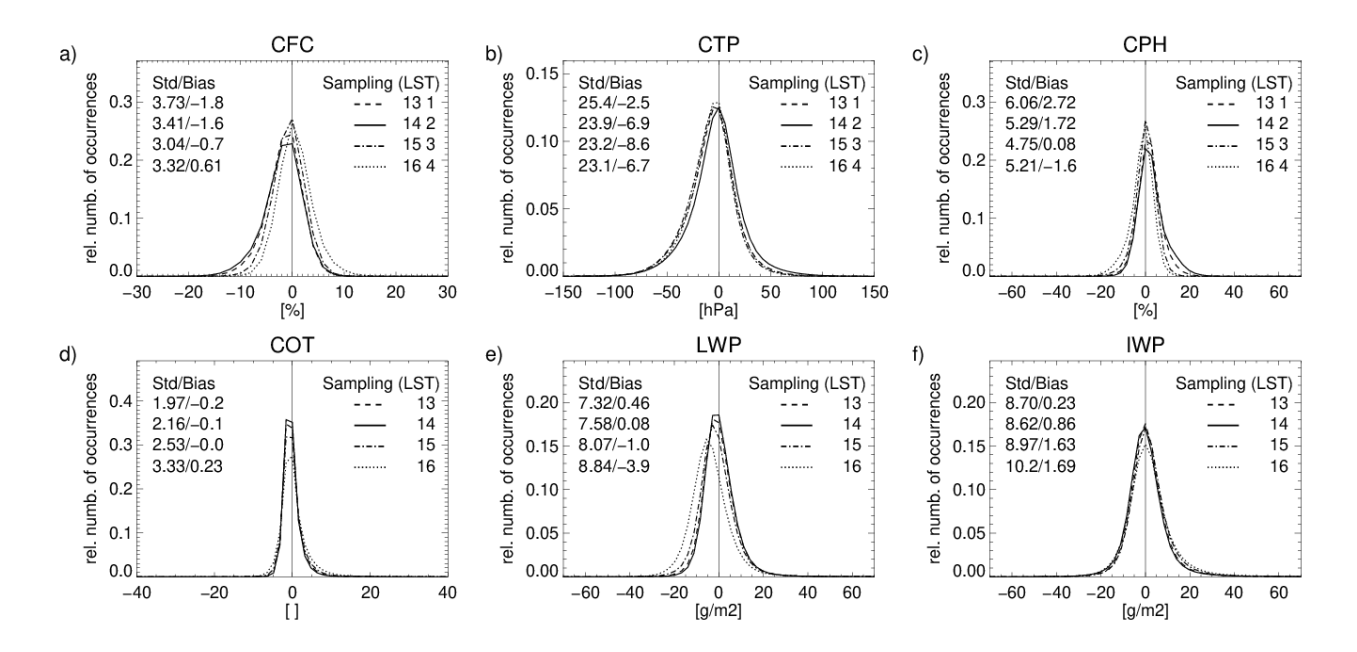


Figure 16: As Figure 15 but for the afternoon overpass times 13:0, 14:00, 15:00 and 16:00.

E3UB

REF: E3UB ISSUE: 1 Revision: 0 DATE: 27/3/2023

PAGE: 22

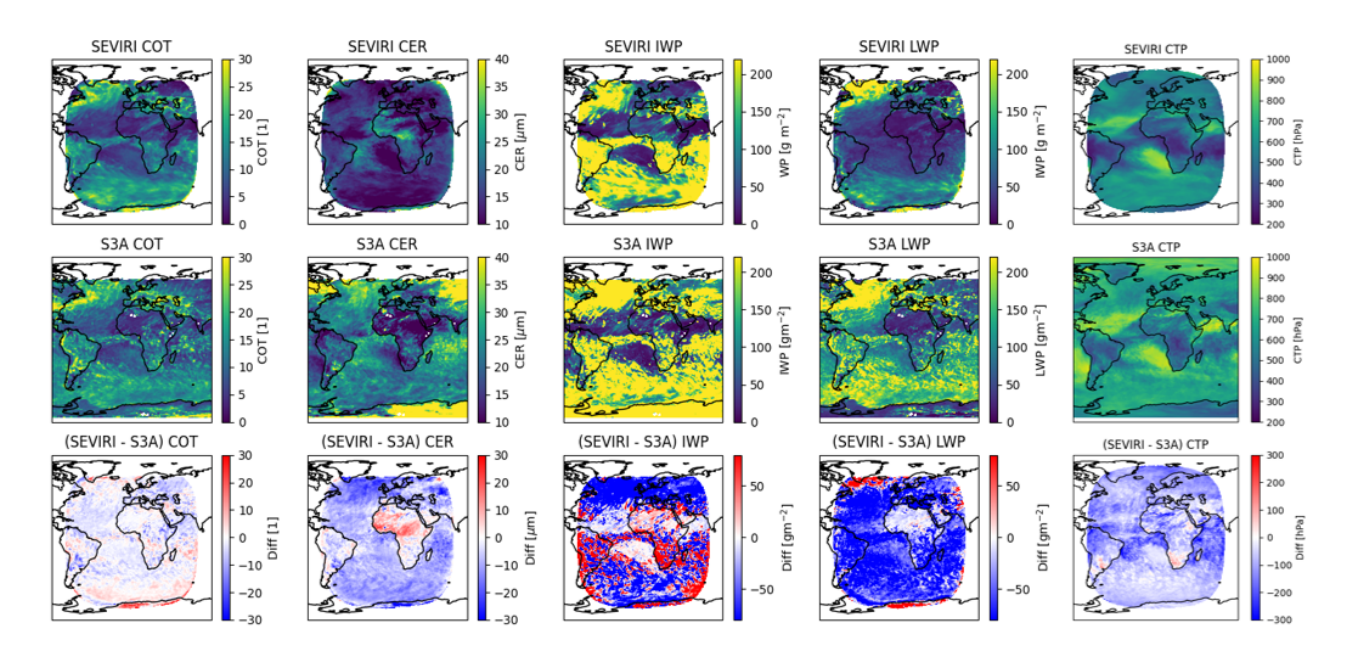


Figure 17: Monthly mean maps of the Cloud_cci cloud products cloud optical thickness (COT), cloud effective radius (CER), cloud ice water path (IWP), cloud liquid water path (LWP) and cloud top pressure (CTP) for SEVIRI (top row), SLSTR (middle row) and their difference (bottom row).

4 Impact of varying spectral characteristics on cloud products

In this section, the impact of small differences in the spectral characteristics of an instrument are assessed using the comparison of SLSTR and SEVIRI. This evaluates both the use of different sets of channels and the use of similar channels with different spectral responses. Monthly mean products are considered from Metosat 11 and Sentinel 3A. It is important to note that the processing of these instruments use basically identical auxiliary data streams and sampling uncertainty estimates as inputs. Hence, the differences discussed are attributed to the differences in spectral characteristics. This is not true for the cloud fraction and phase, so those variables are excluded from this analysis.

Figure 17 shows monthly mean maps (for February 2019) for core cloud properties derived from SEVIRI and SLSTR alongside their differences. For COT, the differences are relatively small (with SEVIRI returning smaller values than SLSTR). For CER, we find higher values for SEVIRI over land (i.e. over Northern Africa) while over ocean SLSTR typically has higher CER. It is generally expected that the SLSTR data used here have higher CER as the 1.6 μm channel is used instead of the 3.8 μm channel used for the SEVIRI retrievals. Using the 1.6 μm channel, however, has the drawback of being contaminated by reflectance at the surface for thinner clouds. This might explain the lower SLSTR CER values over land. LWP and IWP are calculated from COT and CER and are not further discussed here, in part because the different phase retrievals prevent clear conclusions. Monthly mean CTP is higher in the SLSTR retrievals, which might be a consequence of different cloud mask efficiencies, e.g. for low broken clouds, due to different spectral information but also due to different spatial resolutions. However, it is known that the CTP retrievals benefit from inclusion of the CO₂ absorption channel in SEVIRI retrievals, especially in providing improved CTP data, which is likely one of the reasons for the observed differences in SEVIRI-SLSTR CTP. Figure 18 presents scatter plots for the data shown in Figure 17 and Table 15 quantifies the differences found for the full SEVIRI disk.



REF: E3UB ISSUE: 1 Revision: 0 DATE: 27/3/2023

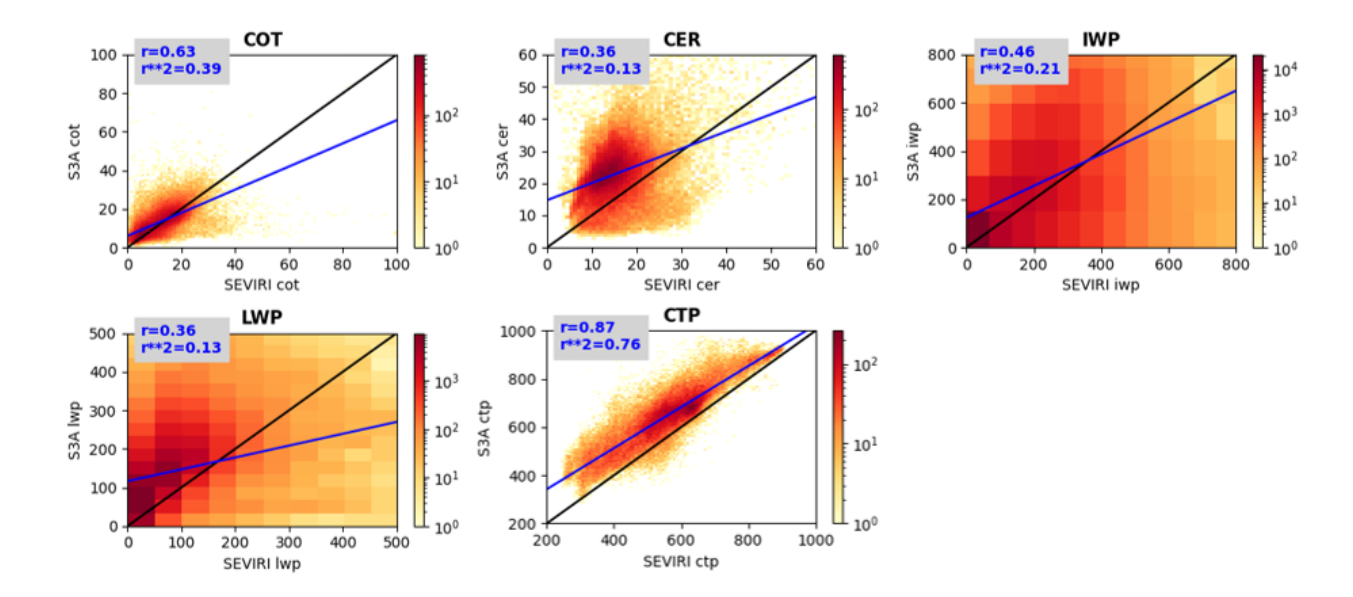


Figure 18: Scatter plots comparing Cloud_cci monthly mean cloud products (as shown in Figure 17) from SEVIRI with SLSTR.

Variable	SEVIRI mean	S3A mean	Bias (SEVIRI-S3A)
CTP [hPa]	551.8	641.9	-90.1
СОТ	12.0	13.2	-1.2
CER [μm]	15.3	23.0	-7.6
IWP [g/m ²]	187.9	249.0	-59.3
LWP [g/m ²]	80.6	140.9	-60.6

Table 15: Mean cloud properties from SEVIRI and SLSTR (as shown in Figure 17) and their differences.

E3UB

REF: E3UB ISSUE: 1 Revision: 0 DATE: 27/3/2023

PAGE: 24

References

- [1] Baum, B. A., Yang, P., Heymsfield, A. J., Bansemer, A., Cole, B. H., Merrelli, A., Schmitt, C., and Wang, C.: Ice cloud single-scattering property models with the full phase matrix at wavelengths from 0.2 to 100 μm, Journal of Quantitative Spectroscopy and Radiative Transfer, 146, 123–139, https://doi.org/10.1016/j.jqsrt.2014.02.029, 2014.
- [2] Feltz, M., Borbas, E., Knuteson, R., Hulley, G., and Hook, S.: The Combined ASTER MODIS Emissivity over Land (CAMEL) Part 2: Uncertainty and Validation, Remote Sensing, 10, 664, https://doi.org/10.3390/rs10050664, 2018.
- [3] Segelstein, David J. The complex refractive index of water. Diss. University of Missouri–Kansas City, 1981.
- [4] Wang, C., Platnick, S., Zhang, Z., Meyer, K., and Yang, P.: Retrieval of ice cloud properties using an optimal estimation algorithm and MODIS infrared observations: 1. Forward model, error analysis, and information content: IR-Based Ice Cloud Retrieval Algorithm, Journal of Geophysical Research: Atmospheres, 121, 5809–5826, https://doi.org/10.1002/2015JD024526, 2016.